mater.scichina.com link.springer.com

Published online 29 March 2022 | https://doi.org/10.1007/s40843-021-1991-6
Sci China Mater 2022, 65(7): 1833–1841

S vacancies in 2D SnS_2 accelerating hydrogen evolution reaction

Gonglei Shao[1,2], Haiyan Xiang[2], Mengjie Huang[3], Yi Zong[4], Jun Luo[5], Yexin Feng[6], Xiong-Xiong Xue[3*], Jie Xu[4,5*], Song Liu[2*] and Zhen Zhou[1]

ABSTRACT **Precise manipulation of atomic defects is essential for modulating the intrinsic properties of two-dimensional (2D) materials. In this study, sulfur (S) atoms are accurately knocked out in the 2D basal plane of pure tin disulfide (SnS_2). By varying the annealing temperatures (250–350°C), SnS_2 with different S vacancy concentrations (Vs-SnS_2) can be obtained. When SnS_2 is annealed at 350°C for 5 h, the S vacancies in the forms of single S atom and double S atoms could reach up to 30.5%. The Vs-SnS_2 is tested in the micro-electrocatalytic hydrogen evolution reaction (HER). Vs-SnS_2 with S vacancies of 30.5% generates superior catalytic performance, with a Tafel slope of 74 mV dec^{-1} and onset potential of 141 mV. The mechanism has been proposed. First, computation confirms that the absence of S atoms prompts surface charge modulation and enhances electronic conductivity. In addition, the under-coordinated Sn atoms adjacent to S vacancy introduce the lattice distortion and charge density redistribution, which are beneficial to hydrogen binding in HER. In short, accurate knockout of specific atoms by controlling the annealing temperature is a promising strategy to explore structure-dependent properties of various 2D materials.**

Keywords: SnS_2, annealing, S vacancy, HAADF-STEM, hydrogen evolution reaction

INTRODUCTION

Two-dimensional (2D) materials exhibit fascinating characteristics with modifiable atomic structure and adjustable electronic structure, providing great potential in the fields of energy storage [1], devices [2], catalysis [3] and optoelectronics [4]. These excellent properties are necessarily associated with atomic structures of 2D materials [5]. According to such structure-activity relationship, the improvement of electronic, catalytic and optical properties of 2D materials has been widely reported [6]. Meanwhile, many strategies on structure adjustments of 2D materials have been developed from both micro-aspect (such as defect engineering [7,8], doping engineering [9], phase engineering [10,11], intercalation engineering [12]) and macro-aspect (such as shape engineering [13], heterostructure construction in horizontal and vertical directions [14–16], size and thickness adjustment [17,18]).

Defect engineering is a vital strategy for managing the microscopic atomic structure, which has been extensively probed and utilized to improve the properties of 2D materials [19–23]. Abundant defect engineering strategies, such as solvothermal synthesis [21], plasma/chemical etching [23,24], template synthesis [21], dealloying and annealing etching [25], have been widely invented. However, there are still many unsolved issues, such as complex fabrication process, indistinct defect states (defect concentration, defect type, electron valence state of elements, and composition proportion), the indeterminable atomic defect location, and the vague defect formation mechanism. Thereinto, the regulation of atomic defect in the microscopic field is the most exquisite in defect engineering, especially the control of defect concentration.

Atomic defect is distinguished as a limiting state of defect, which can tune the electronic structure and energy levels by the vacancy concentration, thus improving the catalytic property [19,20,25]. At present, the large surface area in plane of 2D materials provides a powerful platform for manipulating atomic defects [7,20]. However, based on current research hotspots, the vacancy regulation methods are still insufficient: first, the concentration of atomic vacancy is still imprecise and unstable [7,8]. In addition, the detection of local charge density change caused by vacancies is still not intuitive enough. As a result, precise means are urgently needed to regulate the vacancy concentration of 2D materials, as well as accurately analyzing their corresponding properties.

Hence, in this study, a facile strategy is proposed to accurately generate atomic defects (S vacancies) in 2D SnS_2. The pristine 2D SnS_2 is firstly grown on a SiO_2/Si substrate according to our previously reported techniques [13]. Then, the 2D SnS_2 sample is

[1] Engineering Research Center of Advanced Functional Material Manufacturing of Ministry of Education, School of Chemical Engineering, Zhengzhou University, Zhengzhou 450001, China
[2] Institute of Chemical Biology and Nanomedicine (ICBN), State Key Laboratory of Chemo/Biosensing and Chemometrics, College of Chemistry and Chemical Engineering, Hunan University, Changsha 410082, China
[3] School of Physics and Optoelectronics, Xiangtan University, Xiangtan 411105, China
[4] Institute of Functional Nano and Soft Materials (FUNSOM), Jiangsu Key Laboratory for Carbon-Based Functional Materials & Devices, Soochow University, Suzhou 215123, China
[5] School of Materials Science and Engineering, Tianjin University of Technology, Tianjin 300384, China
[6] Hunan Provincial Key Laboratory of Low-Dimensional Structural Physics and Devices, School of Physics and Electronics, Hunan University, Changsha 410082, China
* Corresponding authors (emails: xxxue@xtu.edu.cn (Xue XX); jiexu@suda.edu.cn (Xu J); liusong@hnu.edu.cn (Liu S))

annealed at different temperatures (250–350°C), which can accurately knock out S atoms from 2D SnS_2 crystals and control the S vacancy concentrations. The formation of SnS_2 with S vacancies in single S atom and double S atoms (Vs-SnS_2) is characterized with aberration-corrected high-angle annular dark-field scanning transmission electron microscopy (HAADF-STEM). The absence of S atoms prompts the change of surrounding electric charge density and stimulates the catalytic activity of the SnS_2 in basal plane. On this account, the electrocatalytic hydrogen evolution reaction (HER) efficiency of Vs-SnS_2 is tested in the microdevice. The most superior catalytic performance can be obtained in Vs-SnS_2 with 30.5% S vacancies, with a Tafel slope of 74 mV dec^{-1} and onset potential of 141 mV. The mechanism may be that S vacancy sites of 2D Vs-SnS_2 can introduce gap states, contributing to hydrogen binding for HER. This defect engineering strategy is not only suitable for 2D materials, but also available for the atom-level structure adjustment of other nanomaterials.

EXPERIMENTAL SECTION

Preparation of SnS_2 with different S vacancy concentrations

The pristine SnS_2 was firstly grown according to our previously reported chemical vapor deposition (CVD) techniques [13]. The grown pure SnS_2 was placed in the middle of a new quartz tube. The system was first ventilated with 100 standard cubic centimeter per minute (sccm) Ar and 5 sccm H_2 for 10 min to remove the impurities in the tube and maintain an inert atmosphere. This system continued to ventilate with this mixture of gases. The furnace was heated to the specified temperature (250 and 350°C) within 60 min in this atmosphere, and the annealing temperature was kept for 5 h, followed by slowly cooling to room temperature. SnS_2 with different S vacancy concentrations can be achieved by adjusting the annealing temperatures.

Device fabrication

2D SnS_2 products with different S vacancy concentrations on SiO_2/Si substrates were spin-coated with a SPR-220-3a photoresist at 4000 r min^{-1} for 60 s, and baked at 115°C for 90 s. Subsequently, the prepared SiO_2/Si substrate was patterned by ultraviolet and deposited with In/Au (10 nm/50 nm) by thermal evaporation to connect the square pad and the nanosheets. Residual photoresist was removed by acetone following a lift-off process, and the final metallic electrode wafer was obtained. Furthermore, in the microelectrocatalytic process, a layer of photoresist was spin-coated on the SiO_2/Si wafer with evaporated metallic electrode, and then exposed with proper ultraviolet beam to open a window on the target position of a nanosheet. The residual photoresist helped to protect the device and avoid unfavorable effect from the Au electrode and another nanosheet.

Electrochemical measurements

After the device was fabricated, the micro-electrocatalysis performance was tested by a three-electrode system using a CHI 660E electrochemical workstation. The exposed area of the nanosheet served as the working electrode, a Pt filament with a diameter of 0.6 mm served as the counter electrode, and self-made saturate Ag/AgCl electrode served as reference electrode. The HER activity of polarization curve was evaluated in 0.5 mol L^{-1} H_2SO_4 electrolyte by linear sweep voltammetry at a scan rate of 5 mV s^{-1}. All reported potential was converted to reversible hydrogen electrode (RHE) potential.

Characterization techniques

The morphology of the samples was observed by optical microscopy (Nikon H600L). Raman spectra were obtained by Horiba Instruments INC (1024X256-OE) equipped with a 532 nm laser excitation and a charge-coupled device (CCD) detector in a backscattering geometry. The photoluminescence (PL) was obtained by using a 325 nm laser excitation. X-ray diffractometer (XRD) measurements of the catalyst were performed on a Bruker D8 advance system. The surface morphology was examined with an atomic force microscope (AFM, Bruker Dimension Icon). HAADF-STEM images and energy dispersive X-ray spectroscopy (EDS) mapping were acquired by the FEI Titan Cubed Themis G2 300 with a probe corrector and a monochromator at 200 kV. The X ray photoelectron spectrometer (XPS) spectra of these samples were analyzed by ESCALAB 250Xi XPS equipped with a monochromatic Al Kα source (λ = 1486.6 eV). The adventitious C 1s peak of ~284.8 eV was used for charging corrections.

RESULTS AND DISCUSSION

Fig. 1a displays the annealing treatment process for manufacturing S atom vacancies on 2D SnS_2. In a mixed atmosphere composed of 100 sccm Ar gas and 5 sccm H_2, the annealing temperature is kept at 250 or 350°C for 5 h, and then the S atom in the 2D SnS_2 crystal structure relaxedly escapes in the form of H_2S molecule. The annealing temperature and time are crucial for the removal of S atoms and the obtained S vacancy concentration. When the temperature exceeds 400°C, high temperature will directly lead to the decomposition of 2D SnS_2 material. When the annealing temperature is below 200°C, S atoms are difficult to overcome the dissociation energy of crystal structure, and deviate from the SnS_2 atomic lattice. Meanwhile, too long or too short time is equally unfavorable. After repeated experiments, annealing conditions are optimized as 250–350°C for 5 h, which will not cause the atomic structure destruction or decomposition of 2D SnS_2 materials.

Therefore, 2D Vs-SnS_2 with different S vacancy concentrations can be prepared by adjusting the annealing temperature. The atomic structure of SnS_2 without annealing is revealed in the HAADF-STEM image (Fig. 1b), showing the perfect T-phase with hexagonal crystal system [13,25]. With the rise of annealing temperature, S vacancy concentration is successively increased in the STEM images (Fig. 1c, d). These S atoms in the six-member ring are knocked out from 2D SnS_2 atomic structure. The mild temperature could ensure that these S atoms on the plane surface of SnS_2 crystal are slowly and moderately etched by H_2, forming the relatively evenly dispersed S atom vacancies in the whole SnS_2 nanosheets, on the premise that the SnS_2 crystal structure is not damaged. The single S atom vacancy (1S) and double S atom vacancies (0S) will be inevitably formed (Fig. 1c, d).

Density functional theory (DFT) calculations were then performed to fundamentally investigate the change in local charge density of Vs-SnS_2. Fig. 1e–g show the calculated atomic structures and charge density distribution for 2D Vs-SnS_2 with different S vacancy concentrations. Compared with pure SnS_2 with equally distributed charge density (Fig. 1e), the S vacancies in Vs-SnS_2 lead to certain lattice distortion and obvious charge

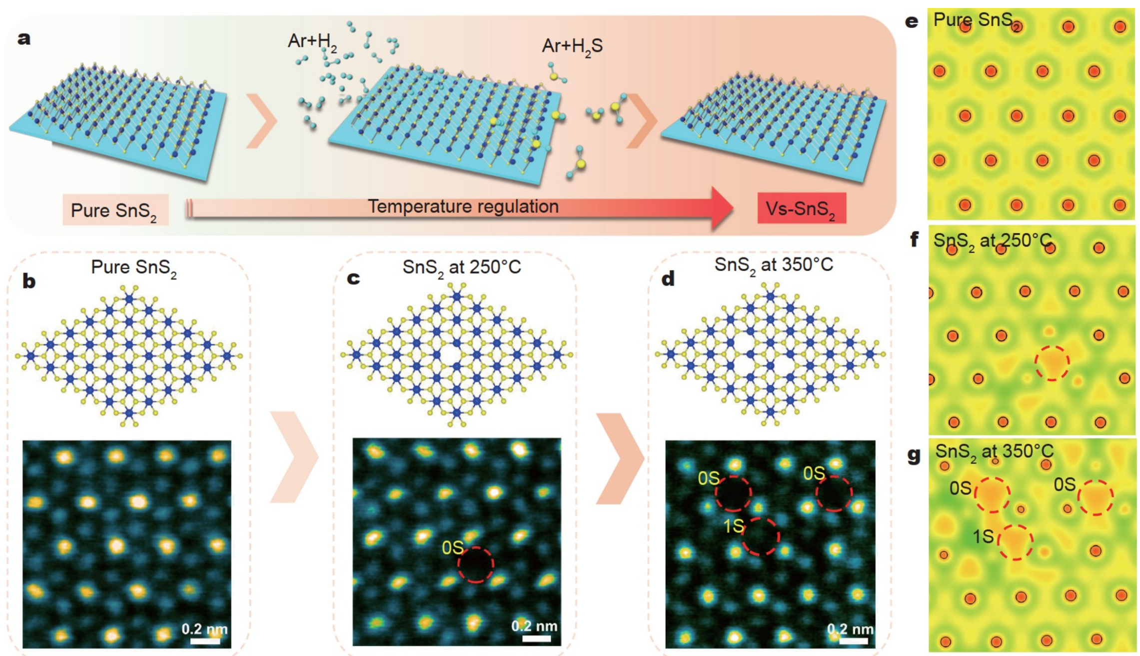

Figure 1 The annealing treatment process of 2D Vs-SnS_2. (a) Vs-SnS_2 with different S vacancy concentrations obtained from the pure SnS_2 annealed at different temperatures. (b–d) Atomic structure schematic diagrams of pure 2D SnS_2, and SnS_2 annealed at 250 and 350°C, and the corresponding atomic resolution HAADF-STEM images. (e–g) Charge density profiles of pure 2D SnS_2, and SnS_2 annealed at 250 and 350°C based on the corresponding HAADF-STEM images.

density redistribution (Fig. 1f, g). Lattice distortion and charge density modulation will inevitably affect the electronic and catalytic properties of 2D Vs-SnS_2. Based on this temperature-dependent annealing, a series of 2D materials with different S vacancy concentrations can be obtained by accurately eliminating S atoms.

With or without annealing treatment, three kinds of 2D SnS_2 samples with different atomic arrangement structures were obtained, including pure SnS_2, SnS_2 annealed at 250°C (denoted as SnS_2 at 250°C), and annealed at 350°C (marked as SnS_2 at 350°C). In Fig. 2a–c, the optical images of pure SnS_2, SnS_2 at 250°C and SnS_2 at 350°C reveal windmill-like 2D morphology [13]. No obvious color and morphology variation is observed from the optical images, revealing no damage and degradation phenomena after annealing (more optical images of the three 2D SnS_2 samples are shown in Fig. S1). Then, AFM was used to characterize the morphology and thickness of pure SnS_2, SnS_2 at 250°C and SnS_2 at 350°C (Fig. 2d–g). No significant change is observed in the morphology and structure of SnS_2 after annealing at different temperatures. However, at 250°C, the thickness of bilayer SnS_2 sample is reduced from 1.51 to 1.38 nm, with a decrease of 0.13 nm. Similarly, at 350°C, the pure bilayer SnS_2 sample is thinned from 1.63 to 1.47 nm, with a decrease of 0.16 nm. Although the 2D SnS_2 samples become thinner after annealing, the original layer number and shape structure are kept, without layer-by-layer thinning. The 2D surface of the Vs-SnS_2 sample becomes cleaner after annealing, which is also in line with the fact that the residual impurities of transferred 2D materials can be cleaned by the annealing treatment [26–28]. Simultaneously, the local stress extension and contraction of the 2D SnS_2 are released with the S atoms escape during annealing [29]. The reduction in thickness further signifies the aggrandizement in the interlayer electron coupling [30]. XRD patterns further prove that the crystallinity of SnS_2 samples is reduced after annealing (Fig. S2), which is mainly derived from the weaker XRD peak intensity, especially the peak intensity of (001) lattice plane (about 15.01°). The weakened (001) peak with feedbacked 2D plane properties indicates that, the S vacancy leads to the uneven structural symmetry in the 2D SnS_2 crystal structure [21].

The variations of microscopic atomic arrangement structure are reflected in Raman and PL spectra. 2D SnS_2 samples with different treatments were characterized with Raman (Fig. 2h). Pure bilayer SnS_2 reveals only a weak out-of-plane vibration Raman signal, namely a broad A_{1g} vibration peak at 316.1 cm^{-1} [13,31]. With the increased annealing temperature, two new vibration peaks appear at 152.5 cm^{-1} (J_1) and 229.6 cm^{-1} (J_2), which are attributed to the extra sporadic vibration centers. These vibration centers come from lattice disorder caused by S atom vacancies [1,25]. Meanwhile, when the annealing temperature increases, a blueshift is gradually observed on the vibration peaks of J_1 and J_2, resulting from more S atom vacancies in the atomic lattice of 2D SnS_2 [1]. Meanwhile, PL analysis was performed for exploring the change of energy band structure induced by the escape of S atom (Fig. 2i). According to the previous tests, the SnS_2 with 1–3 layers showed the indirect bandgap around 2.30 eV [13]. Then the bandgap of 2D SnS_2 after annealing was monitored. The disappearing peak at 2.30 eV indicates that the S vacancy changes the energy band of SnS_2. We further computed the change of density of states (DOS) near the Fermi level caused by different S vacancy concentrations. Fig. 2j shows total and partial DOS for pure SnS_2 and Vs-SnS_2 samples. The increased S vacancy concentration induces obvious gap states, derived from more vacancy levels near the Fermi level for Vs-SnS_2, which increase to the integral DOS. It also endows 2D Vs-SnS_2 with better electronic conductivity than pure SnS_2,

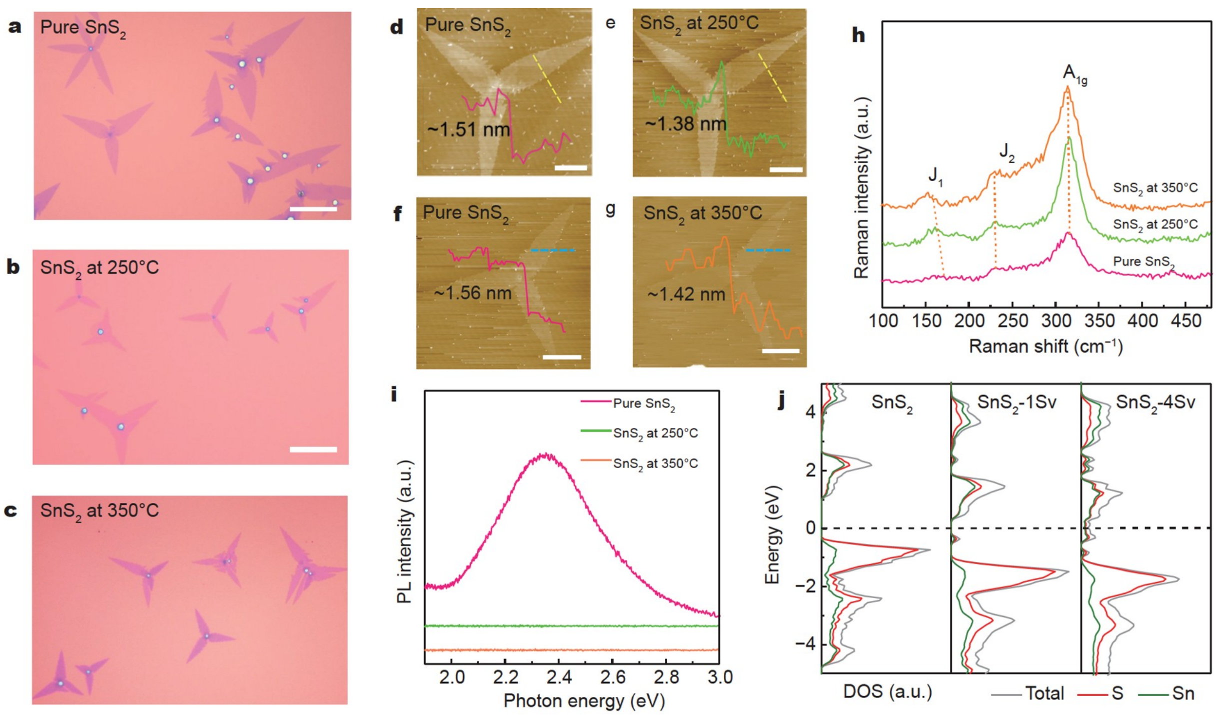

Figure 2 Preparation and basic characterization of 2D SnS_2 with different S vacancy concentrations. Optical images of pure SnS_2 (a), SnS_2 at 250°C (b) and SnS_2 at 350°C (c). Scale bar: 10 μm. AFM images of pure SnS_2 (d, f), SnS_2 at 250°C (e), and SnS_2 at 350°C (g). Scale bar: 5 μm. (h) Raman and (i) PL spectra of pure SnS_2, SnS_2 at 250°C and SnS_2 at 350°C. (j) Computed DOS for pure SnS_2 and Vs-SnS_2 with different numbers of S vacancies in supercell models. The Fermi level is set to zero and marked by black lines.

which will effectively improve the catalytic performance. More comprehensive DOS of more Vs-SnS_2 structures are displayed in Fig. S3, which further confirm the improved integral DOS near the Fermi level with the increase of S vacancy concentration.

Both the identification and quantification of S atom vacancies are indispensable for the performance exploration of 2D SnS_2 materials. XPS, EDS and HAADF-STEM techniques have been applied for characterizing the S atom vacancy of 2D SnS_2. On account of the XPS data (Fig. 3a, b), both Sn and S elements are detected in all 2D SnS_2 samples, where the Sn $3d_{5/2}$ and Sn $3d_{3/2}$ peaks are in line with Sn^{4+}, and the S $2p_{3/2}$ and S $2p_{1/2}$ peaks are assigned to S^{2-} [13,21]. With the increase of annealing temperature, the $3d_{3/2}$ and $3d_{5/2}$ peaks of Sn gradually move towards higher binding energies. The $3d_{3/2}$ peaks of Sn binding energy shift from 494.84 eV (pure SnS_2), 495.17 eV (SnS_2 at 250°C) to 495.59 eV (SnS_2 at 350°C), with peak value offset of 0.75 eV, and $3d_{5/2}$ peaks of Sn binding energy also offset from 486.44 eV (pure SnS_2), 486.57 eV (SnS_2 at 250°C) to 487.19 eV (SnS_2 at 350°C) with a shift of 0.75 eV. Similarly, the S $2p_{3/2}$ and $2p_{1/2}$ peaks also deviate towards the higher binding energy with a shift of 0.3 eV. The high binding energy shift of Sn and S peaks indicates that the annealing treatment causes the escape of S atoms from SnS_2, which affects the local charge density and the binding energy of Sn–S bond [32].

The atomic structures of pure SnS_2 and Vs-SnS_2 samples were further imaged by using HAADF-STEM [7,32,33]. The STEM image reveals that the atomic lattice structure of pure SnS_2 is a hexagonal arrangement of T phase, and the synthesized 2D SnS_2 discloses a perfect single-crystal structure without defects (Fig. S4) [34]. The intensity ratio between brighter and darker spots corresponds to Sn and S atoms. Then, the S atom vacancy is also demonstrated by STEM images (Fig. 3c, d). Abundant S vacancies appear in the atomic structure of 2D SnS_2 annealed at 250 and 350°C. The S atom in the middle of the original six-membered ring has partially disappeared (Fig. 3c, d). Meanwhile, the cross-sectional diagrams of S atom vacancy are sketched by the yellow dotted lines in HAADF images. Sn and S atoms can be clearly identified by the atomic height strength. Even, the 1S and 0S are displayed in Fig. 3e, f, respectively (more STEM images of SnS_2 at 250°C and SnS_2 at 350°C are shown in Figs S5–S7). Whereupon, S atom vacancy can be effectively produced, and the concentration of S vacancies can be accurately controlled by appropriate annealing temperature.

EDS was further used to collect the composition and proportion of all elements in these samples. Except for Sn and S elements, no other element is detected in pure SnS_2, SnS_2 at 250°C and SnS_2 at 350°C (Figs S8–S10). The corresponding EDS element mappings further reveal the uniform distribution of Sn and S atom in a typical SnS_2 sample at 350°C (Fig. 3g). The S/Sn ratios of all SnS_2 samples determined by XPS, EDS and HAADF-STEM are shown in Fig. 3h, and the values obtained by three methods are basically the same [32]. With the increase of annealing temperature, the average S/Sn ratio gradually decreases from 1.99 (pure SnS_2) to 1.60 (SnS_2 at 250°C), and then 1.39 (SnS_2 at 350°C), indicating that the mild temperature promotes S atom to escape from the atomic structure of SnS_2. Hence, the annealing temperature has an influence on the atomic structure stability of 2D SnS_2, and the local S atom vacancy will occur at a relatively low temperature and long time (at 250°C). Moreover, the higher the annealing temperature, the larger the S vacancy concentration, which is gradually increased from 0.5% (pure SnS_2), 20.2% (SnS_2 at 250°C) to 30.5% (SnS_2 at 350°C). This value is higher than that of the S vacancy concentration of many 2D materials, which also demonstrates the

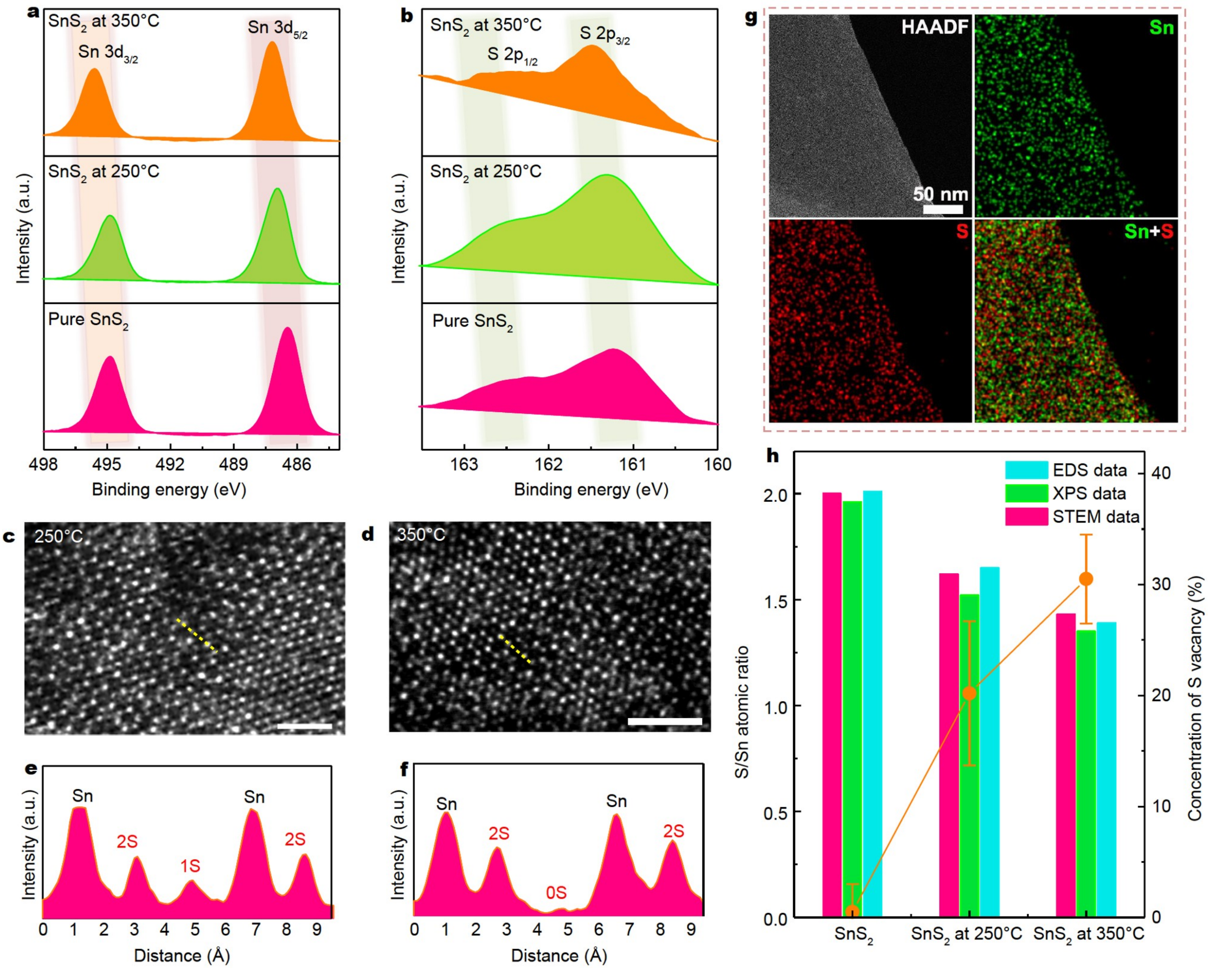

Figure 3 Identification and analysis of S atom vacancy in 2D SnS_2. The XPS data of pure SnS_2, SnS_2 at 250°C and SnS_2 at 350°C: (a) Sn 3d spectra and (b) S 2p spectra. STEM images of (c) SnS_2 at 250°C and (d) SnS_2 at 350°C. Scale bar: 1 nm. The atomic height cross-section diagrams of (e) single S vacancy and (f) double S vacancy come from the corresponding yellow dotted line position of above STEM images. (g) HAADF-STEM image and the corresponding EDS element mappings of SnS_2 at 350°C. (h) Statistical analysis of S/Sn ratio for pure SnS_2, SnS_2 at 250°C and SnS_2 at 350°C based on EDS, XPS and STEM data.

regulation efficiency of the annealing-based strategy [7,32,35].

Then the electrical properties of 2D SnS_2 with different S vacancy concentrations were analyzed by field effect transistors (FETs). Schematic diagram and optical image of an FET device based on SnS_2 at 350°C are presented in Fig. 4a, b, respectively. Pure SnS_2 and Vs-SnS_2 all display typical n-type electrical transmission behaviors (Figs S11–S13). Further, the electrical behaviors of SnS_2 at 250 and 350°C are compared, and the current of SnS_2 at 350°C could not be effectively shut down although the gate voltage (V_g) varies from −60 to 60 V, and the lowest source-drain current (I_{ds}) reaches 15.6 nA (Fig. 4b). At the same time, when the V_{ds} is at 2 V, the I_{ds} is also enhanced with the increased S vacancy concentration (Fig. 4c). The increase of S vacancy also leads to gradually decreased on/off ratio from 213 to 9.37. More S vacancies of 2D SnS_2 provide more surface charge, making it impossible to close the I_{ds} at different gate voltages. With the increase of annealing temperature, a large number of S vacancies appeared in SnS_2. The absence of large amounts of S atoms generates more Sn atoms with unsaturated coordination bond as the active sites, and results in SnS_2 at 350°C having plenty of lone-pair electrons from the Sn atom in 2D limits. These lone-pair electrons bring about more free moving electrons in 2D SnS_2 interlayer. Such much free moving electrons also cause the electrical behavior of SnS_2 at 350°C, and become more n-type. A large number of electrons in the layer cause the current to be unable to turn off under gate voltage. Abundant electrons render the supply of ample electrons in HER, and larger current will be more conducive to the rapid transmission of electrons in the electrocatalytic process. Hence, more electrons derived from S vacancies in SnS_2 at 350°C can improve the HER performance of SnS_2 [32].

Attributed to the excellent active edge site and almost inert base surface, the catalytic activity of 2D materials generally concentrates on the edge, while the base surface with large 2D specific surface area loses its intrinsic value [36]. Therefore, improving the catalytic active sites on the base surface has been the research focus on optimizing the catalytic performance of 2D materials [37]. Among them, increasing S vacancy concentration is crucial to improve the base plane activity of the 2D material, as well as the overall catalytic performance [7]. Here, the overall catalytic performance of 2D SnS_2 with similar morphology is

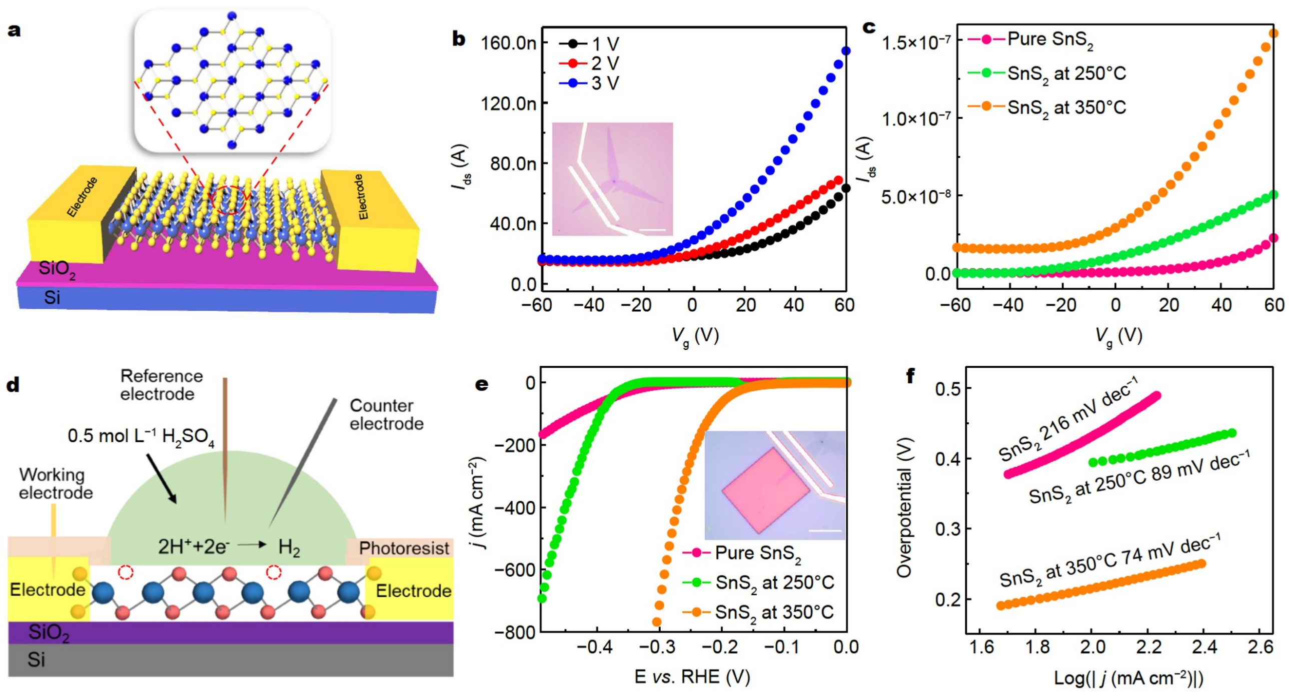

Figure 4 The electrical properties and electrochemical HER of pure SnS_2, SnS_2 at 250°C and SnS_2 at 350°C. (a) Schematic diagram of the FET based on Vs-SnS_2 with different S vacancy concentrations. (b) V_g-I_{ds} curves of SnS_2 at 350°C with V_g from −60 to 60 V. Inset: optical image of the FET device based on SnS_2 at 350°C. Scale bar: 10 μm. (c) Comparison of V_g-I_{ds} curves of pure SnS_2, SnS_2 at 250°C and SnS_2 at 350°C with V_{ds} at 2 V. (d) Schematic diagram of a microreactor. (e) Cathodic polarization curves of the micro-electrochemical reactor fabricated with pure SnS_2, SnS_2 at 250°C and SnS_2 at 350°C. Inset: optical image of the micro-electrochemical reactor with photoresist membrane covering on SnS_2 at 350°C. Scale bar: 10 μm. (f) Corresponding Tafel slopes of different catalysts (overpotential *vs.* log|current density|).

dependent on the S vacancy concentration. A home-made micro-electrochemical reactor was used to test the HER of Vs-SnS_2 (Fig. 4d). Compared with traditional electrochemical testing devices, the micro-electrochemical reactor can accurately detect the change of HER activity in SnS_2 samples with different S vacancy concentrations, thus eliminating the effects of other factors. An optical image of the microreactor device is shown in Fig. 4e. The AFM image of exposed SnS_2 sample in the microreactor with covering photoresist membrane reveals a bilayer thickness (Fig. S14). According to the polarization curve (Fig. 4e), the current density of 2D SnS_2 gradually increases with the rise of annealing temperature. Meanwhile, as another key parameter used to evaluate HER performance, the onset potential was also obtained from cathodic polarization curves. The onset potential gradually decreases from 346 mV (pure SnS_2) to 141 mV (SnS_2 at 350°C) at 10 mA cm^{-2}. The lower onset potential means that a smaller voltage is required to drive SnS_2 to produce H_2.

The HER activity of nanomaterial-based electrocatalysts can be evaluated by comparing their corresponding Tafel slopes. Fig. 4f reveals the Tafel plots of pure SnS_2, SnS_2 at 250°C and SnS_2 at 350°C derived from the corresponding polarization curves. Notably, the value is much lower for SnS_2 at 350°C (74 mV dec^{-1}) compared with pure SnS_2 (216 mV dec^{-1}), suggesting that the catalytic activity is substantially improved by increasing S vacancies. The Tafel slope can be used to qualitatively analyze the electrocatalytic reaction mechanism. The value of 74 mV dec^{-1} for SnS_2 at 350°C indicates a combination of the Volmer reaction and the Heyrovsky reaction. In the Volmer reaction, the initial adsorption of protons from the acid solution to form adsorbed H ($H^+ + e^- \rightarrow H_{ad}$) at the active sites is usually considered to be fast. In the Heyrovsky reaction, a solvated proton from the water layer reacts with one adsorbed surface hydrogen to form H_2 ($H_{ad} + H^+ + e^- \rightarrow H_2$), and the formation of the surface-bound H_2 should dominate the kinetics [21]. The Tafel slope obtained for SnS_2 at 350°C is smaller, confirming that the more S atom vacancies activate more active sites [7,38]. Thus, the high electrical conductivity and abundant active sites (30.5% S vacancies) of SnS_2 at 350°C facilitate fast electron/charge transfer in the HER catalytic process. Meanwhile, the chronoamperometry data of SnS_2 at 350°C indicate the stabilization time of current density is less than 10 min, resulting in the sudden disappearance of the current signal (Fig. S15). The weak stability of SnS_2 at 350°C catalysts may be due to the disengagement between the electrode and the 2D material or the damage of the electrode and the SnS_2 material.

DFT calculations were then performed to fundamentally investigate the enhanced HER performance of Vs-SnS_2. Optimizations of the intrinsic activity and conductivity of Vs-SnS_2 are considered as key factors to improve the HER activity. Fig. 5a–d show the calculated atomic structures and charge density distribution for Vs-SnS_2 with different S vacancy concentrations. Pure SnS_2 exhibits equally distributed charge density (Fig. S16). However, compared with pure SnS_2, the introduction of S vacancies in Vs-SnS_2 structures leads to certain lattice distortion and obvious charge density redistribution, especially for atoms adjacent to vacancies. Lattice distortion and charge density modulation have important effects on electronic and catalytic properties of Vs-SnS_2. The metals generally possess better conductivity than semiconductors, and semiconductor or metal could be well distinguished by analyzing the presence or absence of band gap in the electronic DOS. Therefore, we select the

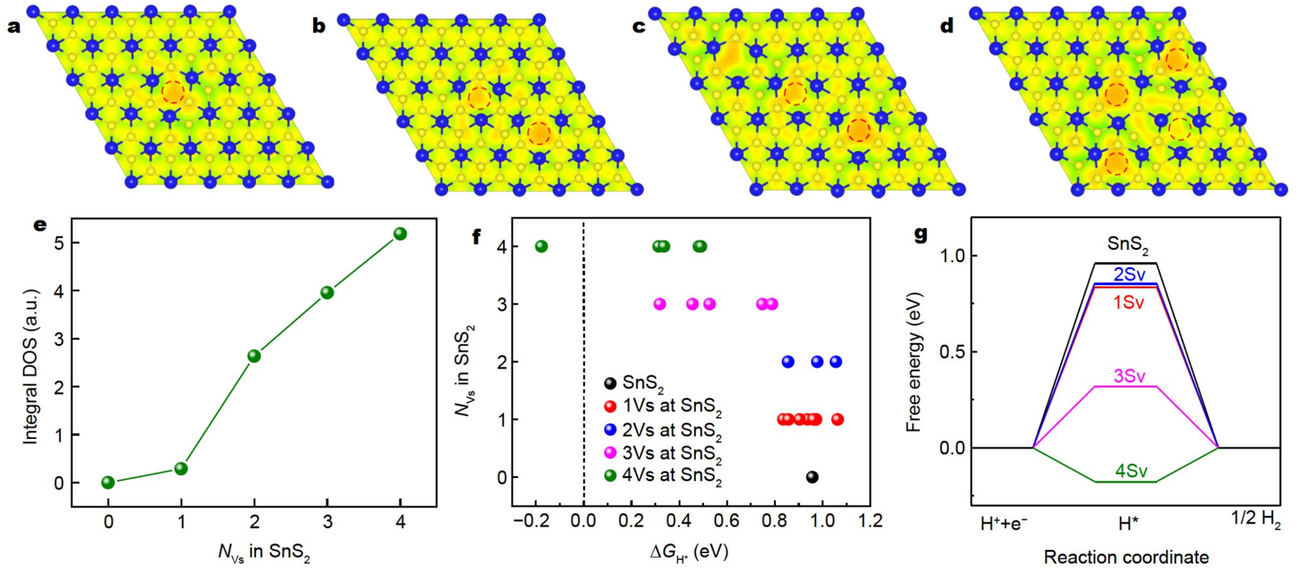

Figure 5 (a–d) Top-view charge density distributions of Vs-SnS_2 with different numbers of S vacancies (N_{Vs}) in theoretically calculated supercells. (e) The integral DOS near the Fermi level for Vs-SnS_2 as the function of N_{Vs}. The integral region includes both of the occupied electronic states and unoccupied states, as shown in blue areas in Fig. S3. (f) ΔG_{H*} *versus* Vs-SnS_2 with different N_{Vs} S vacancies. (g) HER free-energy diagram with optimal ΔG_{H*} for pure SnS_2 and Vs-SnS_2.

integral DOS near the Fermi energy to characterize the semiconductor or metallic properties and the integral region includes both of the occupied electronic states and unoccupied states near the Fermi level, as shown in the blue areas in Fig. S3. Fig. 5e clearly shows that the integral DOS near the Fermi level gradually increases from zero with the increase of S-vacancy concentration in Vs-SnS_2, suggesting the semiconductor-to-metallic transition. Importantly, this transition from semiconductor to metallic properties indicates better electrical conductivity. Finally, surface charge modulation and enhanced electrical conductivity will effectively improve the HER catalytic activity of Vs-SnS_2. The intrinsic catalytic activity of SnS_2 can be optimized by finely tuning the S vacancy concentration.

Gibbs free energy of hydrogen adsorption H* (ΔG_{H*}) on the catalyst surface can be considered as a good indicator to evaluate the HER activity [39]. An ideal HER catalyst is expected to possess a value of ΔG_{H*} close to zero, which can effectively balance the reaction rates of adsorption and desorption steps. Importantly, the ΔG_{H*} on the catalyst surface is a critical factor to directly determine the HER rates. By calculating ΔG_{H*}, the tuning effect of S vacancy concentration on HER catalytic activity of Vs-SnS_2 was further computationally explored. Fig. 5f summarizes the calculated ΔG_{H*} at several active sites of Vs-SnS_2 with diverse S vacancy concentrations. HER free-energy diagrams with the optimal ΔG_{H*} values among all considered active sites for each Vs-SnS_2 are also displayed in Fig. 5g. As seen in Fig. 5f, g, Vs-SnS_2 surfaces exhibit smaller absolute values of ΔG_{H*} close to zero compared with pure SnS_2 surface, indicating better HER performance. Among these Vs-SnS_2 samples, the increase of S vacancy concentration gradually enhances the H* adsorption, thus effectively improving the HER activity in a wide range. These findings are consistent with our experimental results and further prove that moderate vacancy is critical to effectively activate catalytic sites and promote HER reaction. Furthermore, the superiority of single S vacancies over agglomerate S vacancies originates from more effective surface electronic structure engineering. Meanwhile, both vacancy concentration and distribution facilitate the modulation of catalytic performance, which broadens the prospects of vacancy design. Such defect engineering strategy can be further extended to other 2D materials and applied for other catalytic reactions besides HER.

CONCLUSIONS

In summary, an optimal 2D Vs-SnS_2 with different S vacancy concentrations is experimentally realized *via* controlling the annealing temperature. The S atoms are accurately knocked out from the 2D basal plane of pure SnS_2, and the maximum S vacancy concentration can reach up to 30.5% by annealing at 350°C for 5 h. The S atom vacancies are in the form of single and double S atoms. The S vacancy can activate the basal plane of SnS_2 and generate superior catalytic performance. The potential mechanism is that the introduction of S vacancy in Vs-SnS_2 leads to lattice distortion and obvious charge density redistribution near S vacancy. In addition, the under-coordinated Sn atoms caused by S vacancy introduce surface charge modulation and enhance electrical conductivity, which is also beneficial to hydrogen evolution. As a result, the intrinsic catalytic activity of SnS_2 can be optimized by tuning the S vacancy concentrations. The proposed facile strategy of defect engineering is promising in enhancing catalytic performance of 2D materials in other reactions besides HER.

Received 16 November 2021; accepted 8 February 2022; published online 29 March 2022

1 Shao G, Lu Y, Hong J, *et al.* Seamlessly splicing metallic $Sn_xMo_{1-x}S_2$ at MoS_2 edge for enhanced photoelectrocatalytic performance in micro-reactor. Adv Sci, 2020, 7: 2002172

2 Schulman DS, Arnold AJ, Das S. Contact engineering for 2D materials and devices. Chem Soc Rev, 2018, 47: 3037–3058

3 Xu Y, Jiang X, Shao G, *et al.* Interface effect of Ru-MoS_2 nanoflowers on lignin substrate for enhanced hydrogen evolution activity. Energy En-

viron Mater, 2021, 4: 117–125
4 Alzakia FI, Tan SC. Liquid-exfoliated 2D materials for optoelectronic applications. Adv Sci, 2021, 8: 2003864
5 Guo HW, Hu Z, Liu ZB, *et al.* Stacking of 2D materials. Adv Funct Mater, 2021, 31: 2007810
6 Su L, Fan X, Yin T, *et al.* Inorganic 2D luminescent materials: Structure, luminescence modulation, and applications. Adv Opt Mater, 2020, 8: 1900978
7 Wang X, Zhang Y, Si H, *et al.* Single-atom vacancy defect to trigger high-efficiency hydrogen evolution of MoS_2. J Am Chem Soc, 2020, 142: 4298–4308
8 Xiong J, Di J, Xia J, *et al.* Surface defect engineering in 2D nanomaterials for photocatalysis. Adv Funct Mater, 2018, 28: 1801983
9 Loh L, Zhang Z, Bosman M, *et al.* Substitutional doping in 2D transition metal dichalcogenides. Nano Res, 2021, 14: 1668–1681
10 Li W, Qian X, Li J. Phase transitions in 2D materials. Nat Rev Mater, 2021, 6: 829–846
11 Xu X, Pan Y, Liu S, *et al.* Seeded 2D epitaxy of large-area single-crystal films of the van der Waals semiconductor 2H $MoTe_2$. Science, 2021, 372: 195–200
12 Stark MS, Kuntz KL, Martens SJ, *et al.* Intercalation of layered materials from bulk to 2D. Adv Mater, 2019, 31: 1808213
13 Shao G, Xue XX, Zhou X, *et al.* Shape-engineered synthesis of atomically thin 1T-SnS_2 catalyzed by potassium halides. ACS Nano, 2019, 13: 8265–8274
14 Zhang L, Tang Y, Khan AR, *et al.* 2D materials and heterostructures at extreme pressure. Adv Sci, 2020, 7: 2002697
15 Wang X, Pan L, Yang J, *et al.* Direct synthesis and enhanced rectification of alloy-to-alloy 2D type-II $MoS_{2(1-x)}Se_{2x}/SnS_{2(1-y)}Se_{2y}$ heterostructures. Adv Mater, 2021, 33: 2006908
16 Xu X, Han B, Liu S, *et al.* Atomic-precision repair of a few-layer 2H-$MoTe_2$ thin film by phase transition and recrystallization induced by a heterophase interface. Adv Mater, 2020, 32: 2000236
17 Hu D, Zhao T, Ping X, *et al.* Unveiling the layer-dependent catalytic activity of $PtSe_2$ atomic crystals for the hydrogen evolution reaction. Angew Chem Int Ed, 2019, 58: 6977–6981
18 Cui F, Wang C, Li X, *et al.* Tellurium-assisted epitaxial growth of large-area, highly crystalline ReS_2 atomic layers on mica substrate. Adv Mater, 2016, 28: 5019–5024
19 Shi R, Zhao Y, Waterhouse GIN, *et al.* Defect engineering in photocatalytic nitrogen fixation. ACS Catal, 2019, 9: 9739–9750
20 Xie J, Yang X, Xie Y. Defect engineering in two-dimensional electrocatalysts for hydrogen evolution. Nanoscale, 2020, 12: 4283–4294
21 Shao G, Xue Xx, Wu B, *et al.* Template-assisted synthesis of metallic 1T'-$Sn_{0.3}W_{0.7}S_2$ nanosheets for hydrogen evolution reaction. Adv Funct Mater, 2020, 30: 1906069
22 Zheng YJ, Chen Y, Huang YL, *et al.* Point defects and localized excitons in 2D WSe_2. ACS Nano, 2019, 13: 6050–6059
23 Liang Q, Zhang Q, Gou J, *et al.* Performance improvement by ozone treatment of 2D $PdSe_2$. ACS Nano, 2020, 14: 5668–5677
24 Zhang P, Xiang H, Tao L, *et al.* Chemically activated MoS_2 for efficient hydrogen production. Nano Energy, 2019, 57: 535–541
25 Xu J, Lai S, Hu M, *et al.* Semimetal 1H-SnS_2 enables high-efficiency electroreduction of CO_2 to CO. Small Methods, 2020, 4: 2000567
26 Wang P, Song S, Najafi A, *et al.* High-fidelity transfer of chemical vapor deposition grown 2D transition metal dichalcogenides *via* substrate decoupling and polymer/small molecule composite. ACS Nano, 2020, 14: 7370–7379
27 Wakafuji Y, Moriya R, Masubuchi S, *et al.* 3D manipulation of 2D materials using microdome polymer. Nano Lett, 2020, 20: 2486–2492
28 Kim K, Yankowitz M, Fallahazad B, *et al.* Van der Waals heterostructures with high accuracy rotational alignment. Nano Lett, 2016, 16: 1989–1995
29 Wang W, Zhou L, Hu S, *et al.* Visualizing piezoelectricity on 2D crystals nanobubbles. Adv Funct Mater, 2021, 31: 2005053
30 Shao G, Xue XX, Liu X, *et al.* Twist angle-dependent optical responses in controllably grown WS_2 vertical homojunctions. Chem Mater, 2020, 32: 9721–9729
31 Ye G, Gong Y, Lei S, *et al.* Synthesis of large-scale atomic-layer SnS_2 through chemical vapor deposition. Nano Res, 2017, 10: 2386–2394
32 Zhang X, Liao Q, Kang Z, *et al.* Hidden vacancy benefit in monolayer 2D semiconductors. Adv Mater, 2021, 33: 2007051
33 Bai F, Xu L, Zhai X, *et al.* Vacancy in ultrathin 2D nanomaterials toward sustainable energy application. Adv Energy Mater, 2020, 10: 1902107
34 Gong Y, Yuan H, Wu CL, *et al.* Spatially controlled doping of two-dimensional SnS_2 through intercalation for electronics. Nat Nanotech, 2018, 13: 294–299
35 Jin H, Li L, Liu X, *et al.* Nitrogen vacancies on 2D layered W_2N_3: A stable and efficient active site for nitrogen reduction reaction. Adv Mater, 2019, 31: 1902709
36 Wang Z, Li Q, Xu H, *et al.* Controllable etching of MoS_2 basal planes for enhanced hydrogen evolution through the formation of active edge sites. Nano Energy, 2018, 49: 634–643
37 Deng D, Novoselov KS, Fu Q, *et al.* Catalysis with two-dimensional materials and their heterostructures. Nat Nanotech, 2016, 11: 218–230
38 Ge J, Zheng JY, Zhang J, *et al.* Controllable atomic defect engineering in layered $Ni_xFe_{1-x}(OH)_2$ nanosheets for electrochemical overall water splitting. J Mater Chem A, 2021, 9: 14432–14443
39 Greeley J, Jaramillo TF, Bonde J, *et al.* Computational high-throughput screening of electrocatalytic materials for hydrogen evolution. Nat Mater, 2006, 5: 909–913

Acknowledgements This work was supported by the National Natural Science Foundation of China (22175060 and 21975067) and the Natural Science Foundation of Hunan Province, China (2021JJ10014 and 2021JJ30092). Feng Y acknowledges the support from the National Natural Science Foundation of China (11974105), the National Basic Research Program of China (2016YFA0300901). Xu J acknowledges the support from the Natural Science Foundation of Jiangsu Province, China (BK20210729), and the Collaborative Innovation Center of Suzhou Nano Science and Technology, the 111 Project and the Joint International Research Laboratory of Carbon-Based Functional Materials and Devices. The computational resources were provided by the supercomputer TianHe in Changsha, China.

Author contributions Shao G and Xu J conceived the research. Shao G designed the experiments. Shao G and Xiang H performed the experiments and data analysis. Xue XX and Huang M contributed to the DFT simulation. Xu J, Zong Y, and Luo J performed STEM characterizations. Shao G, Xue XX, Feng Y, Zhou Z, Xu J and Liu S contributed to manuscript editing. Shao G, Liu S and Xue XX wrote the manuscript. All authors contributed to the general discussion.

Conflict of interest The authors declare that they have no conflict of interest.

Supplementary information Supporting data are available in the online version of the paper.

Gonglei Shao received his PhD degree in chemistry from Hunan University in 2021. He joined the School of Chemical Engineering, Zhengzhou University as a researcher. At present, he is mainly engaged in the design and properties of novel 2D transition metal sulfide catalysts, the preparation of large-area 2D materials by chemical vapor deposition, and the preparation of ternary or multivariate 2D alloy materials.

Xiong-Xiong Xue received his PhD degree in physics from Hunan University in 2020. He is currently an associate professor at the School of Physics and Optoelectronics, Xiangtan University. His research concerns novel physical properties and applications of low-dimensional materials.

Jie Xu received his PhD degree from the School of Materials Science and Engineering, Tianjin University of Technology in 2020. Now he is a lecturer at the Institute of Functional Nano and Soft Materials (FUNSOM), Soochow University, China. His current interests include two-dimensional materials and electron microscopy research.

Song Liu received his PhD degree in 2011 from Peking University. He was a postdoctoral fellow working in Prof. Liming Dai's group (2011–2013) in Case Western Reserve University. After three years research at the National University of Singapore (2013–2016), he is now a full professor at the Institute of Chemical Biology and Nanomedicine, Hunan University. His research interests focus on the controlled synthesis of low-dimensional materials, the application research of functional devices and nano biological research.

富含S空位的二维SnS_2加速析氢反应

邵功磊[1,2], 向海燕[2], 黄梦婕[3], 宗怡[4], 罗俊[5], 冯页新[6], 薛雄雄[3*], 许杰[4,5*], 刘松[2*], 周震[1]

摘要 精确调控二维平面内的原子缺陷可有效调节二维材料的各种基本性质. 本研究通过改变退火温度(250–350°C), 实现了二维二硫化锡(SnS_2)基面上硫(S)原子的精确敲除, 得到了具有不同S空位浓度的SnS_2(Vs-SnS_2). 当SnS_2 在350°C下退火5 h时, 大量出现单S原子和双S原子空位形态, S空位浓度可达30.5%. 在自制微芯片中测试了Vs-SnS_2的电催化析氢性能. S空位浓度达到30.5%的Vs-SnS_2表现出优异的催化性能, Tafel斜率达到74 mV dec^{-1}, 起始电位低至141 mV. 通过理论计算对反应机制进行研究, 结果表明, S原子的缺失促进了表面电荷调制, 提高了SnS_2的导电性. 此外, S空位导致Sn原子的不饱和配位, 从而引起晶格畸变和电荷密度重新分布, 更加有利于析氢反应. 简而言之, 通过控制退火温度可精确敲除特定原子、制造缺陷, 可成为探索各种2D材料结构相关特性的一种有效策略.